Simultaneously Improving Tabletability and Solubility of Diclofenac by Cocrystallization with Picolinamide

Chenyu Wu,[a] Zijian Wang,[b] Xu Han,[a] Xinyi Yu,[a] Changquan Calvin Sun,[b*] Zhengzheng Zhou[a*]

[a] NMPA Key Laboratory for Safety Evaluation of Cosmetics, Guangdong Provincial Key Laboratory of Tropical Disease Research, Department of Hygiene Inspection & Quarantine Science, School of Public Health, Southern Medical University, Guangzhou, Guangdong 510515, China

[b] Pharmaceutical Materials Science and Engineering Laboratory, Department of Pharmaceutics, College of Pharmacy, University of Minnesota, Minneapolis, MN 55455, USA

*To whom correspondence should be addressed:

Dr. Zhengzheng Zhou, E-mail: zhouzz418@smu.edu.cn

Prof. Dr. Changquan Calvin Sun, E-mail: sunx0053@umn.edu

Abstract

Diclofenac (DIC) is a nonsteroidal anti-inflammatory drug with poor tabletability and water solubility. In the present study, a new diclofenac-picolinamide cocrystal (DIC-PIC) was prepared to simultaneously improve its tabletability and solubility. The cocrystal was characterized using multiple techniques, such as X-ray diffraction, thermal methods and spectral analyses. The tabletability of DIC-PIC was significantly improved over DIC, which is attributed to the larger bonding area between crystals due to the higher plasticity of DIC-PIC, demonstrated by the lower in-die mean yield pressure, $P_{y,i}$, of DIC-PIC (59.5 ± 0.6 MPa) than DIC (86.6 ± 1.4 MPa). The higher plasticity of DIC-PIC is consistent with the existence of a slip plane (001) in its crystal structure. The thermodynamic solubility of DIC-PIC is significantly higher than that of DIC (112 times higher in water and 22 times higher in pH = 6.8 buffer solution). Hence, the simultaneous improvement in tabletability and solubility of DIC-PIC overcomes two main barriers in developing DIC tablets, which makes it a promising candidate for developing a DIC tablet with improved performance.

Keywords: Diclofenac; cocrystal; tabletability; solubility

1. Introduction

Cocrystals are solid forms composed of two or more compounds in the same crystal lattice with a specific stoichiometry held together by non-covalent bonds, such as hydrogen bonds, π-π stacking interactions, van der Waals forces and halogen bonds. A pharmaceutical cocrystal contains molecules of at least one active pharmaceutical ingredient (API). Pharmaceutical cocrystals facilitate drug development by presenting improved properties over their parent compounds (Bolla et al., 2022, Shaikh et al., 2018), including mechanical properties (Chow et al., 2012, Karki et al., 2009, Zhou et al., 2016a), solubility (Chettri et al., 2024, Varshosaz et al., 2018), stability (Hao et al., 2022, Xu et al., 2015), permeability (Diniz et al., 2020, Kumari et al., 2024, Pandey et al, 2024), bioavailability (Dai et al., 2023, Zhou et al.,2019, Zhou et al., 2020), and therapeutic efficacy (Wang et al, 2022). The tablet is currently the most commonly used dosage form due to its small volume, good stability, flexibility with drug dose, low manufacturing cost, and high production throughput (Gupta et al., 2009, Perumalla and Sun, 2014, Sun, 2009). Sub-optimal mechanical properties of APIs hinder the successful development of tablets for high dose APIs. Such a challenge, however, also presents an opportunity for employing cocrystallization as an API crystal engineering to enable successful tablet development.

Diclofenac (DIC, Scheme 1) is a nonsteroidal anti-inflammatory drug (NSAID) widely used for treating acute and chronic arthritis, rheumatoid arthritis, ankylosing spondyloarthritis, and other related diseases. However, DIC faces two main challenges in developing a high quality tablet: 1) poor tabletability, with tablet tensile strength not exceeding 1 MPa (Ramirez et al., 2010); and 2) low aqueous solubility (6.06 μg/mL at 25 ℃ in pH 4.77 water, Llinas et al., 2007), which limits its oral bioavailability (Semalty et al., 2009). Numerous studies have been carried out to improve the solubility of DIC through cocrystallization and salt formation (Feng et al., 2021, Gaitano et al., 2016, Goswami et al., 2020, Nugrahani et al., 2018, Surov et al., 2014). A DIC sodium salt is used in the marketed DIC tablet due to its high solubility. However, this salt forms a hydrate under high humidity, potentially impacting the manufacturing process, storage conditions, and the performance of the final product (Bartolomei, 2007). Additionally, problems due to poor mechanical strength have been reported for diclofenac tablets (Ramirez, 2010). A previous study

showed that the solubility of clotrimazole-diclofenac cocrystal in pH 1.2 buffer solution was 31 times higher than that of DIC (Drozd et al., 2023). Cocrystallization was also shown to have the ability to improve tabletability of APIs (Mannava et al., 2021). Thus, simultaneous enhancement of both the tabletability and solubility of DIC through cocrystallization is an appealing possibility, which is the goal of this study to realize.

In selecting suitable coformers, we considered amide due to their ability to form acid-amide heterodimers with carboxylic acid groups through N-H···O=C and O-H···O=C hydrogen bonding (Saha and Desiraju, 2018). Hence, we evaluated five amides as cocrystal formers (Figure S1 and Table S1) and successfully synthesized a 1:1 diclofenac-picolinamide cocrystal, which simultaneously exhibited improved tabletability and solubility compared to DIC.

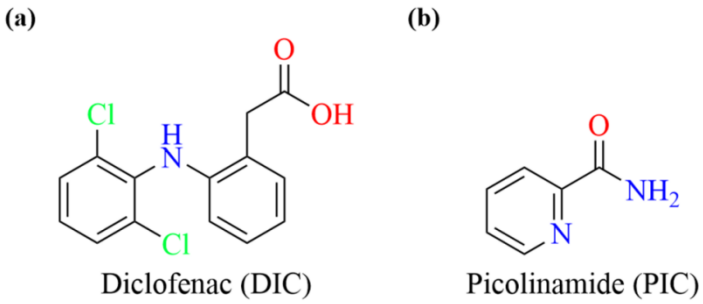

Scheme 1. Chemical structures of a) Diclofenac (DIC) and b) Picolinamide (PIC).

2. Materials and methods

2.1. Materials

DIC and PIC were purchased from Aladdin Biochemical Technology Co. Ltd. (Shanghai, China) with purity ≥98% by HPLC analysis. Acetonitrile (spectrophotometric grade) and methanol (spectrophotometric grade) were purchased from Merck KGaA (Darmstadt, Germany). All materials were used as received without further purification. Ultra-pure water with a resistivity greater than 18.2 MΩ.cm, produced by Milli-Q Element A10 Purification System (Darmstadt, Germany), was used in this work.

2.2. Preparation of DIC-PIC (1: 1) cocrystal

2.2.1. Slow solvent evaporation method (Single crystal cultivation)

A total of 20.0 mg of DIC and 50.0 mg of PIC were accurately weighed and mixed in a 10 mL

centrifuge tube, to which 2.0 mL of acetonitrile was added, followed by 30 min sonication to fully dissolve the solids. After cooling, the solution was passed through a 0.22 μm filter membrane into a 10 mL vial, which was sealed with parafilm, into which 2 to 3 holes were introduced to allow slow solvent evaporation at room temperature to obtain single crystals.

2.2.2. Liquid assisted grinding method (Bulk powder preparation)

Approximately 0.708 g of DIC and 0.292 g of PIC (1:1 molar ratio) were weighed, mixed, and placed in an agate mortar. Then, after adding 4 drops of acetonitrile, the mixture was ground using a pestle until dry to obtain a bulk powder.

2.3. Solid state characterizations

2.3.1. Single crystal X-ray diffraction (SCXRD)

A Rigaku XtaLAB Pro Diffraction Supernova Dual Source instrument (Tokyo, Japan) was used to obtain the X-ray diffraction data using a Mo K_α radiation source ($\lambda = 0.71073$ Å) at 180 K. Olex2 (Dolomanov et al., 2009) was used to solve the structure and SHELXTL (Sheldrick, 2015) was used to refine the molecular structure model, using full-matrix least squares on F^2 principles. All non-hydrogen atoms were refined with anisotropic displacement parameters. Hydrogen atoms were added in "idealized" positions and refined as riding atoms with relative isotropic displacement parameters. These steps were repeated until the refinement converged.

2.3.2. Powder X-ray diffraction (PXRD)

The diffraction pattern of the cocrystal powder was obtained via a Rigaku powder X-ray instrument (Tokyo, Japan), operating at 40 kV and 150 mA using Cu K_α radiation source ($\lambda =$ 1.54056 Å). The powder after screening was scanned in the range of 5° - 40° with a step size of 0.02°. To evaluate the phase purity of bulk powder, experimental PXRD pattern was compared with the simulated PXRD pattern calculated from the solved crystal structure using Mercury software (version 2020.1).

2.3.3. Thermal analyses

Differential scanning calorimetry (DSC) and thermogravimetric analysis (TGA) were used to analyze the thermal behaviors of materials (Schultheiss and Newman, 2009, Zhou et al., 2016b) to determine if a new phase is generated. The onset temperatures of all the investigated

substances were determined by DSC (DSC 6000, PerkinElmer, Waltham, USA). Approximately 3 - 5 mg of a sample was added to a hermetically sealed aluminum pan and heated from 30 °C to the decomposition temperature of the sample with a heating rate of 10 °C/min under nitrogen purge (50 mL/min). An empty pan identically prepared was used as a reference.

Approximately 5 - 10 mg of each of the samples was characterized on a DSC/TGA 1 analyzer (Mettler Toledo, Switzerland), heated from 30 °C to 500 °C under nitrogen purge (50 mL/min) at a heating rate of 10 °C/min. STARe Evaluation software 13.0 was used to analyze the weigh loss data.

2.3.4. Fourier transformation infrared spectrum (FT-IR)

FT-IR was used as a means of determining whether a cocrystal is formed by identifying characteristic absorption bands of functional groups between 400 - 4000 cm^{-1}. At first, 150 mg of KBr was ground to a fine powder, and then 1 - 2 mg of a sample was mixed with KBr powder, followed by further grinding to uniformly distribute the sample. The mixture was then compacted for one minute at 20 MPa hydraulic pressure using a 769YP-15A tablet press machine (Tianjin Keqi, China) to form a uniformly translucent disc, which was placed on a suitable carrier and detected by a Bruker Vertex 70 spectrometer (Karlsruhe, Germany). A KBr disc was used as a blank.

2.3.5. True density

The true density of powders was measured using a helium pycnometer (Quantachrome Instruments, Ultrapycnometer 1000e, Byonton Beach, FL, USA). The sample cell was filled with accurately weighed powder (1 - 2 g). The measurement was stopped when the coefficient of volume variation of the last five consecutive measurements was less than 0.005%. Otherwise, the experiment was automatically terminated after a maximum of 50 measurements (Goldenberg et al., 2023).

2.3.6. Surface morphology analysis

Sample surface morphology was analyzed using a EM-30AX+ scanning electron microscopy (SEM, COXEM, Tokyo), operated at 15 kV voltage and 56 μA emission current. All samples were first passed through a 150 μm sieve (mesh 100), mounted onto a double-faced adhesive tape, and

then sputtered-coated with gold using an ion sputtering instrument. Image acquisition and analysis were performed using COXEM-30AX+3.1.5 software.

2.4. Compaction properties

All powders were passed through a 90 μm sieve (mesh 170) before being compacted at pressures ranging from 20 MPa to 350 MPa on a compaction simulator (Styl'One, Medelpharm, Beynost, France), simulating a Korsch XL 100 press at 20 rpm (corresponding to 103 ms of dwell time). MgSt spray (Styl'One Mist, Medelpharm, Beynost, France) was used to lubricate the die wall and punch tips before each compaction. Tablet dimensions were measured using a digital caliper. Subsequently, tablets were diametrically broken using a texture analyzer (TA-XT2i; Texture Technologies Corporation, Scarsdale, NY) at a speed of 0.005 mm/s with a 5 g trigger force. Tablet tensile strength was calculated from the maximum breaking force and tablet dimensions using Eq. (1), following a standard procedure (Fell and Newton, 1970).

$$\sigma = \frac{2F}{\pi d h} \quad (1)$$

where F is breaking force, d is tablet diameter, and h is tablet thickness.

Tablet porosity (ε) was calculated from the tablet apparent density (ρ) and material true density (ρ_t) using Eq. (2).

$$\varepsilon = 1 - \frac{\rho}{\rho_t} \quad (2)$$

Tabletability was characterized by plotting tablet tensile strength against compaction pressure; compressibility was characterized by plotting porosity against compaction pressure, and compactibility was characterized by plotting tablet tensile strength against porosity.

In-die Heckel analysis was conducted by following a standard procedure (Vreeman and Sun, 2021). In-die mean yield pressure, $P_{y,i}$, was the reciprocal of the slope of the linear portion of the in-die Heckel plot using Eq. (3),

$$-\ln(\varepsilon) = \frac{1}{P_{y,i}} P + A \quad (3)$$

where P is the compaction pressure, and A is a constant. The measurement was performed in triplicate.

2.5. Solubility and intrinsic dissolution rates (IDRs)

2.5.1. Solubility

The solubility of DIC and DIC-PIC cocrystal was determined in both water and a pH 6.8 buffer solution. The pH 6.8 buffer solution was prepared following the method outlined in the Chinese Pharmacopoeia. Briefly, 250 mL of a 0.2 M potassium dihydrogen phosphate solution was mixed with 118 mL of a 0.2 M sodium hydroxide solution, and the mixture was diluted with water to a final volume of 1000 mL. To measure solubility of DIC, approximately 60 mg of DIC was suspended in 3 mL of a target medium in a 20 mL vial. The vial was tightly capped and shaken at 100 rpm on a constant-temperature shaker at 37 °C for 72 hours. The supernatant was then passed through a 0.22 μm nylon filter membrane before concentration determination using HPLC. Three samples were prepared in parallel for each medium. The residual solid was analyzed by PXRD for phase identification. Solubility of DIC-PIC cocrystal could not be directly measured in aqueous media due to spontaneous dissociation into DIC during the course of the experiment. Hence, its thermodynamic solubility was determined using a modified procedure where DIC-PIC (60 mg) was co-equilibrated with PIC (240 mg) to suppress phase change of DIC-PIC. PXRD patterns suggest that DIC-PIC cocrystal during the thermodynamic solubility experiment remained phase stable (Figure S2). In this scenario, the thermodynamic solubility of the DIC-PIC cocrystal can be calculated using Eq. (4) (Good and Rodríguez-Hornedo, 2009),

$$S_{cocrystal} = \sqrt[\alpha+\beta]{\frac{K_{sp}}{\alpha^{\alpha}\beta^{\beta}}} = \sqrt[\alpha+\beta]{\frac{[A]^{\alpha}[B]^{\beta}}{\alpha^{\alpha}\beta^{\beta}}} \quad (4)$$

where α and β represent the stoichiometric coefficients of the cocrystal components (= 1 for both α and β). [A] and [B] are the concentrations of DIC and PIC, respectively.

An HPLC instrument (Shimadzu Prominence LC-20A) with Agela Venusil XBP C18 chromatographic column (150 mm × 4.6 mm, 5 μm) was used to measure the concentration of DIC and PIC in each sample. Based on the actual condition of the instrument, the previously reported HPLC method (Li et al., 2023, Hiew et al., 2019) was modified. As for DIC, the mobile phase contained 0.1% acetic acid water and acetonitrile at a volume ratio of 45:55. The wavelength of the UV detector was set at 276 nm. As for PIC, the mobile phase contained 0.1%

acetic acid water and acetonitrile at a volume ratio of 92 : 8. The wavelength of the UV detector was set at 254 nm. The temperature was set at 25 ℃, and the flow rate of the mobile phase was set at 1 mL/min with an injection volume of 10 μL.

2.5.2. IDRs

A dissolution apparatus (Huanghai SY-3D, Shanghai, China) was employed to measure IDR. Approximately 100 mg of each sample was weighed, placed in a compression mold with a circular hole of 5.8 mm diameter and compressed with a hydraulic pressure of 2 MPa for 15 s. Only one face of the compact was exposed to the medium (500 mL pure water), maintained at 37.0 ℃ and stirred by a paddle rotating at 100 rpm, while all other surfaces were coated with wax. Approximately 2 mL of sample solution was collected at 1, 3, 5, 7, 9 and 13 min and the same volume of pure water (pre-warmed to 37.0 ℃) was supplemented. All the withdrawn liquid samples were filtered through a 0.22 μm nylon filter membrane into 10 mL glass vials separately. The tablet surface exposed to dissolution medium was analyzed by PXRD after IDR experiment.

2.6. Dynamic vapor sorption (DVS)

Moisture sorption and desorption measurements were performed to characterize hygroscopicity using a DVS Intrinsic instrument (London, UK). Approximately 25 mg of each sample was weighed and placed in a DVS-HT pan under nitrogen purge at 25.0 ℃. The relative humidity (RH) was increased from 0% to 90% in 10% increments and then to 95%. The desorption experiment was conducted in reverse RH order to complete a 0%-95%-0% cycle for each powder. The criterion for reaching equilibrium moisture content at each RH step was set at a mass change rate of ≤0.002% per minute. The residual solid was then analyzed by PXRD to identify any phase changes.

2.7. Computational calculations

2.7.1. Crystal structure visualization and attachment energy calculation

Mercury software (version 2020.1) was used to visualize crystal structures and calculate attachment energies (Wang et al., 2019). Crystal structure visualization helps identify the slip plane in crystals. Attachment energy (E_{att}), which is the energy released by a single layer of thickness d_{hkl} attaching to a crystal surface (h k l) during crystal growth, was calculated using the

Dreiding force field and the E_{vjen} electrostatic correction (Sun and Kiang, 2008). The slip plane was considered to be the crystallographic planes with the lowest E_{att}, implying that the weakest interaction energy between slip planes.

2.7.2. Energy framework

Energy framework graphically quantifies the intermolecular interactions among molecules in a crystal structure, where the radius of the cylinder is proportional to the energy (Wang et al., 2018). CrystalExplorer17 (Mackenzie et al., 2017, Spackman et al., 2021) was used to calculate the intermolecular interaction energies, based on B3LYP-D2/6-31G(*d,p*) molecular wavefunctions. The energy framework was constructed for a selected molecule with all surrounding molecules with any atom within 3.8 Å of that molecule. The total intermolecular interaction energy is decomposed into electrostatic, polarization, dispersion, and exchange-repulsion components with scale factors of 1.057, 0.740, 0.871, and 0.618, respectively. The inter-layer or intra-layer interaction energies were the sum of the interaction energy between a given molecule in a layer and all interacting molecules in an adjacent layer or in the same layer, respectively. The cutoff threshold was set at 4 kJ/mol.

3. Results and discussion

3.1. Crystal structure analysis

The result of SCXRD experiment confirmed the formation of a DIC-PIC cocrystal, which belongs to the $P\bar{1}$ space group of the triclinic system (Table 1), with each asymmetric unit containing one DIC and one PIC (Figure 1a). Table S2 lists the geometrical parameters of hydrogen bonds.

Table 1. The main crystallographic parameters of DIC-PIC cocrystal.

Formula	$C_{14}H_{11}Cl_2NO_2{\cdot}C_6H_6N_2O$	Crystal system	Triclinic
Molecular weight	418.26	Space group	$P\bar{1}$
T (K)	179.99 (10)	ρ_{calcd} (g/cm^3)	1.464
a (Å)	7.5294 (7)	θ range	2.458 to 29.536
b (Å)	8.3451 (9)	Unique reflections	4387

c (Å)	15.2879 (11)	R_{sigma}	0.0543
a (°)	95.380 (7)	R_1 [I>2σ(I)]	0.0485
β (°)	96.055 (7)	wR_2 (all)	0.1207
γ (°)	93.482 (8)	Goodness-of-fit	1.029
V (Å^3)	948.60 (15)	CCDC number	2342400

A PIC molecule and a DIC molecule form a DIC-PIC dimer through $R_2^2(8)$ hydrogen bonding interactions (O2-H2···O3, 2.566 Å and N2-H2A···O1, 2.943 Å) (Figure 1a). The basic structural unit consisted of two DIC-PIC dimers, connected by $R_4^2(8)$ hydrogen bonding pattern, consisting of hydrogen bonds formed between N2-H2A and N2-H2B of a molecule of PIC with O1 of two neighboring DIC molecules (Figure 1b). Such structural units form a chain structure through C18-H18···C7 (3.558 Å) and C18-H18···C8 (3.732 Å) short contacts, running along the b axis (Figure 1c). The chains form a layer through halogen bonds (C11-H11···Cl2, 3.629 Å) between H11 of DIC of each structural unit and Cl2 of DIC of a neighboring structural unit (Figure 1c).

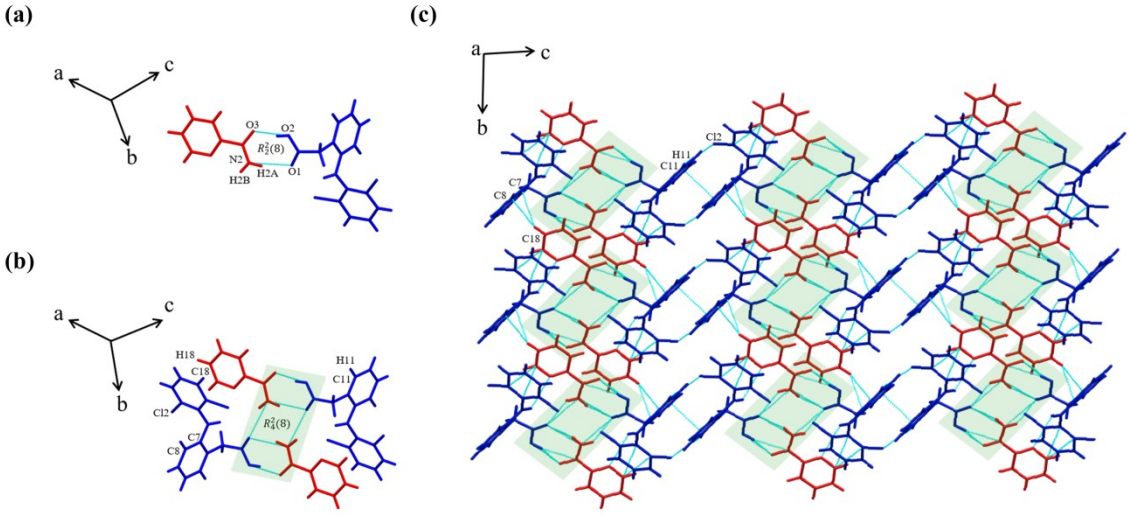

Figure 1. The packing diagrams of DIC-PIC cocrystal: (a) an asymmetric unit with hydrogen bonds shown; (b) a basic structural unit; (c) layer structure. Red = PIC, Blue = DIC.

3.2. PXRD analysis

The characteristic diffraction peaks of DIC (9.2°, 17.7°, 18.6°, 20.5°, 23.5°, 24.3°, 29.9° and 30.5° 2θ) and PIC (10.7°, 20.5°, 25.1° and 28.1° 2θ), were not observed in the PXRD pattern of the DIC-PIC cocrystal powder (Figure 2). The DIC-PIC cocrystal also exhibited new diffraction peaks

at 5.5°, 12.2°, 15.3°, 16.1°, 25.7°, 25.9° and 32.9° 2θ. To verify the phase purity of the cocrystal powder, the experimental PXRD pattern was compared with the simulated PXRD pattern. The two patterns are similar except peaks in the experimental PXRD pattern shift to the lower 2θ value (Figure 2). This peak shift is attributed to the thermal expansion of the lattice (Chen et al., 2019), since the experimental PXRD pattern was obtained at 298.0 K, while the simulated PXRD pattern was solved at 180.0 K.

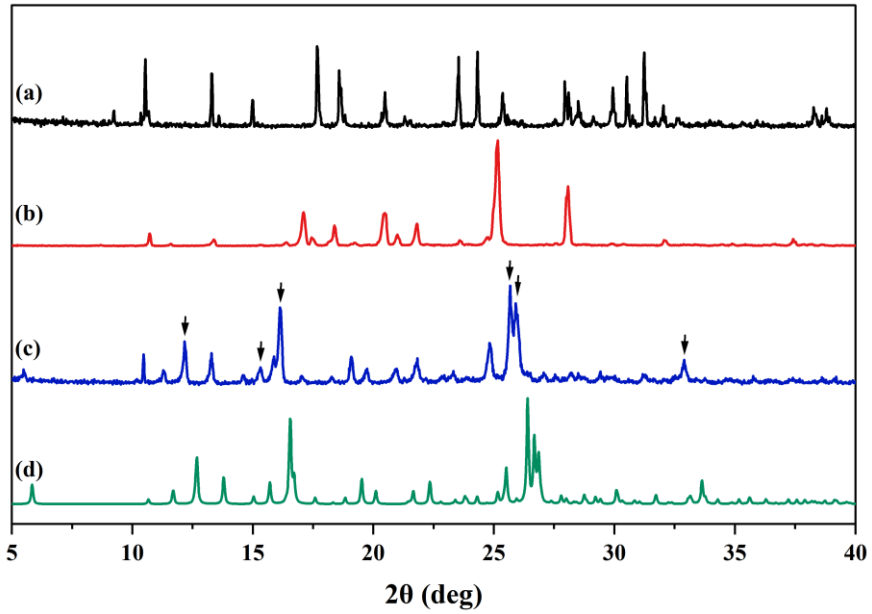

Figure 2. PXRD patterns of (a) DIC, (b) PIC, (c) experimental DIC-PIC cocrystal and (d) calculated DIC-PIC cocrystal.

3.3. Thermal analyses

The TGA curves of all samples showed little mass loss before their corresponding onset melting temperatures (171.9 °C for DIC, 106.1 °C for PIC, and 134.6 °C for DIC-PIC (Figure 3, Table 2). The corresponding melting enthalpy are 87.1 J/g (DIC), 109.5 J/g (PIC) and 66.2 J/g (DIC-PIC) (Table 2). The small endothermic event at 68.7 °C in the DSC thermograms of PIC before the melting corresponds to the known polymorph II to polymorph I phase transformation (Evora et al., 2012). The melting temperature of DIC-PIC cocrystal is between the two starting materials, showing the same trend observed in some other cocrystal systems (Perlovich, 2015).

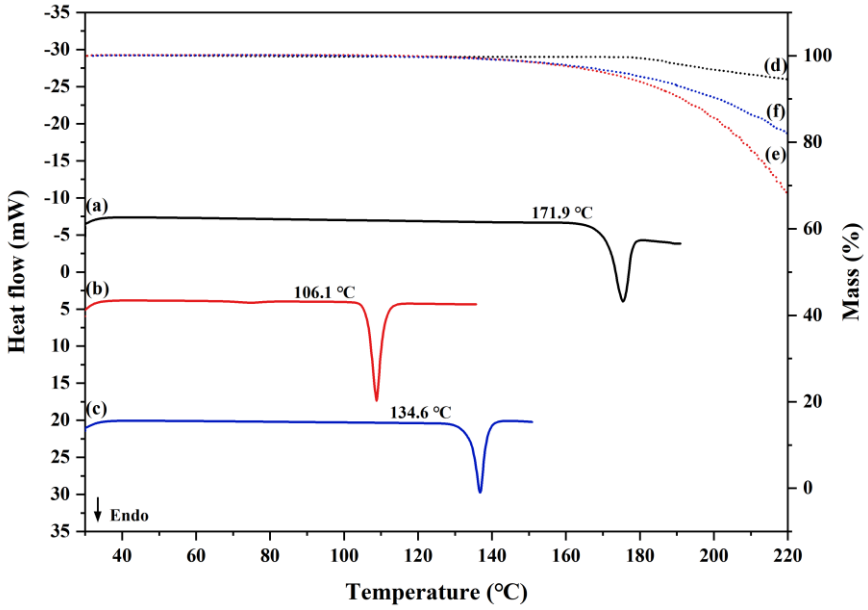

Figure 3. DSC thermograms of (a) DIC, (b) PIC and (c) DIC-PIC cocrystal and TGA thermograms of (d) DIC, (e) PIC and (f) DIC-PIC cocrystal.

Table 2. Thermal properties of DIC, PIC, and the DIC-PIC cocrystal (mean ± SD, n=3).

Compounds	Onset melting temperature (°C)	Enthalpy of fusion (J/g)
DIC	171.9 ± 0.2	87.1 ± 0.2
PIC	106.1 ± 0.1	109.5 ± 2.4
DIC-PIC cocrystal	134.6 ± 0.1	66.2 ± 0.2

3.4. FT-IR

The FT-IR spectrum of DIC shows three characteristic absorption peaks appeared in 3323 cm^{-1}, 1694 cm^{-1} and 937 cm^{-1} (Figure 4), which are attributed to the stretching vibration of O-H, C=O, and out-of-plane bending vibration of O-H (Pireddu et al., 2018). The PIC spectrum shows peaks corresponding to the asymmetric (3419 cm^{-1}) and symmetric stretching (3277 cm^{-1} and 3176 cm^{-1}) vibration of N-H and stretching vibration of C=O (1663 cm^{-1}). In the case of the DIC-PIC cocrystal, the absorption peaks of O-H for DIC shifts to 3354 cm^{-1}, and the out-of-plane bending vibration of O-H disappears, which is attributed to the elimination of the carboxylic acid dimer interactions present in DIC (Castellari and Ottani, 1997, Hui et al., 2001). Moreover, the

asymmetric stretching vibration of N-H on PIC shifts from 3419 cm^{-1} to 3427 cm^{-1}, while the symmetric stretching vibration appears at 3260 cm^{-1}. The blue shift of the O-H absorption and N-H stretching peaks is because these functional groups are involved in weaker hydrogen bonds in the cocrystal than those in DIC and PIC (Lemmerer et al., 2013, Joseph and Jemmis, 2007). The stretching vibration of the C=O bond shifted to 1687 cm^{-1} in the DIC-PIC cocrystal, probably due to conjugation between C=O on PIC and O-H on DIC (Smith, 2018). Furthermore, the stretching vibrations of DIC and PIC resulted in a series of broad peaks in the hydrogen bond area (2300 cm^{-1} to 2600 cm^{-1}), which is consistent with previous studies (Aakeröy et al., 2011, Mukherjee et al., 2013). A wide and low intensity absorption peak appear at 1921 cm^{-1}, caused by the simultaneous excitation of the in-plane bending vibration of C-H, which is in the ortho-position to the -COOH group on the benzene ring of the DIC molecule, and the out-of-plane bending vibration of the N-H group in PIC (Surov et al., 2018).

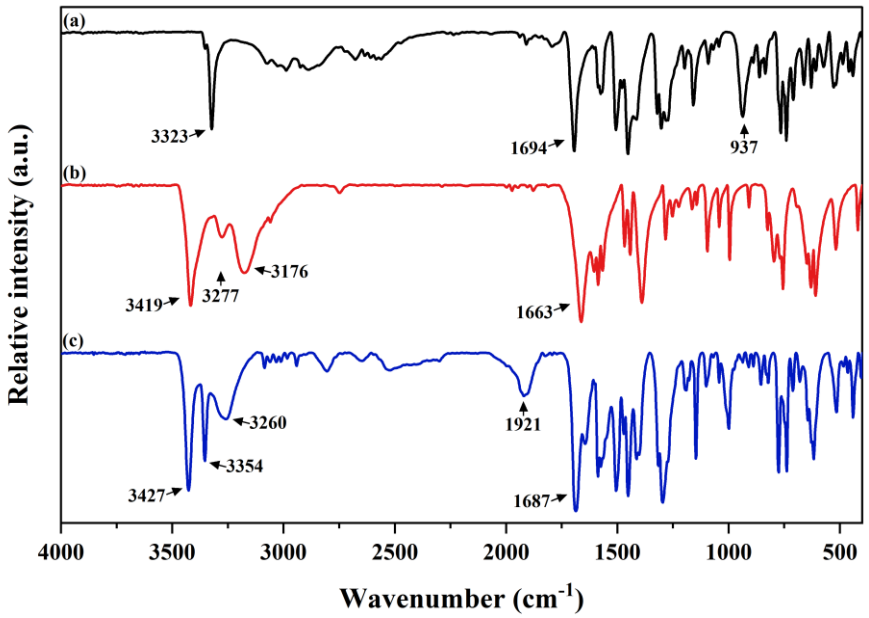

Figure 4. FT-IR spectra of (a) DIC, (b) PIC and (c) DIC-PIC cocrystal.

3.5. Compaction properties

The tabletability is the ability of the powder to be compressed into a tablet with a specific strength at a given compaction pressure (Sun, 2017, Yadav et al., 2017). A higher tensile strength at the same compaction pressure suggests a better tabletability (Joiris et al., 1998). The

292 tabletability of DIC, PIC, DIC-PIC, and a physical mixture of DIC and PIC (PM, 1:1 molar ratio)
293 followed a descending order of PIC > DIC-PIC > PM > DIC (Figure 5). The tabletability of DIC is
294 very poor, yielding only weak tablets at pressures below 80 MPa, which is consistent with the
295 literature (Ramirez, 2010). The DIC-PIC cocrystal exhibited significantly better tabletability
296 compared to both the DIC and the physical mixture, with the maximum tensile strength of up to
297 1.8 MPa at 150 MPa. The tensile strength of DIC-PIC cocrystal tablets decreases when the
298 compaction pressure exceeds 150 MPa, indicating the occurrence of overcompression (Wang et
299 al., 2017).

300 The tabletability is an outcome of interparticulate bonding area (BA) – bonding strength (BS)
301 interplay, wherein the BA is influenced by mechanical properties, particulate properties, as well
302 as tableting conditions, while BS is determined by the nature of a given material (Sun, 2011).
303 Compressibility and compactibility profiles are commonly used to assess the BA and BS,
304 respectively (Modi et al., 2014, Patel et al., 2006, Sun and Kleinebudde, 2016, Sun 2009). However,
305 they should be used with caution in mixtures due to the formation of the complex contact between
306 particles with different mechanical properties (Wang et al., 2024). Due to insufficient data points
307 of DIC and physical mixture, only the compressibility and compactibility profiles of PIC and DIC-
308 PIC were analyzed. PIC tablets exhibited a lower porosity than that of DIC-PIC cocrystal across the
309 entire compaction pressure range studied (Figure 6a), indicating a better compressibility. Thus,
310 under the same compaction pressure, PIC developed larger BA than DIC-PIC corresponding to
311 lower tablet porosity. On the other hand, the tensile strength at zero porosity (σ_0), extrapolated
312 from compactibility profiles using the Ryshkewitch-Duckworth model (Duckworth, 1953;
313 Ryshkewitch, 1953; Sun, 2005), was used to compare BS assuming BAs were the same at zero
314 porosity. Comparable σ_0 values were obtained, suggesting similar BS values (Figure 6b).
315 Therefore, the larger BA and similar BS of PIC results in better tabletability of PIC than DIC-PIC
316 cocrystal.

317 When particle size and shape are not significantly different, larger BA is formed between
318 particles of a more plastic material. Based on the plasticity parameter $P_{y,i}$ value (Table 3), the
319 plasticity of the three materials follows a descending order of PIC > DIC-PIC > DIC. This rank

order is the same as that of tabletability, indicating that BA dominates the BA-BS interplay. The least plastic DIC experienced limited plastic deformation under compression, leading to insufficient BA and the worst tabletability. Based on $P_{y,i}$ values, PIC ($P_{y,i}$ = 50.8 ± 0.4 MPa) and DIC-PIC ($P_{y,i}$ = 59.5 ± 0.6 MPa) have plasticity in the vicinity of microcrystalline cellulose (MCC) ($P_{y,i}$ = 54.2 ± 1.5 MPa) (Wang et al., 2023), which is known to be a plastic pharmaceutical excipient. The higher plasticity of PIC than DIC-PIC is also consistent with the slightly higher compressibility of PIC, resulting in a larger BA and higher tabletability, especially at pressures > 150 MPa (Figure 5).

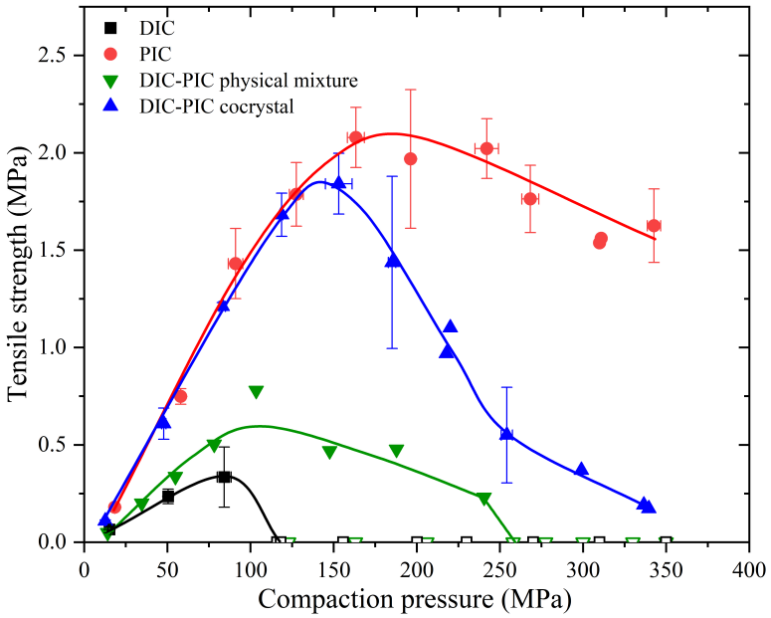

Figure 5. Tabletability profiles of DIC, PIC, DIC-PIC cocrystal and DIC-PIC physical mixture (n = 3).

The DIC, PIC, and DIC-PIC crystals exhibit distinct morphological characteristics, where DIC crystals are prism-shaped, PIC crystals are plate-like, and DIC-PIC crystals are irregularly shaped (Figure 7). The DIC-PIC crystals are also significantly smaller than those of DIC and PIC, which would have contributed to the tabletability of DIC-PIC by effectively increasing BA. Despite this, tabletability of PIC is still better than DIC-PIC, implying that the effect of higher plasticity of PIC outplayed the effect of smaller particle size of BA.

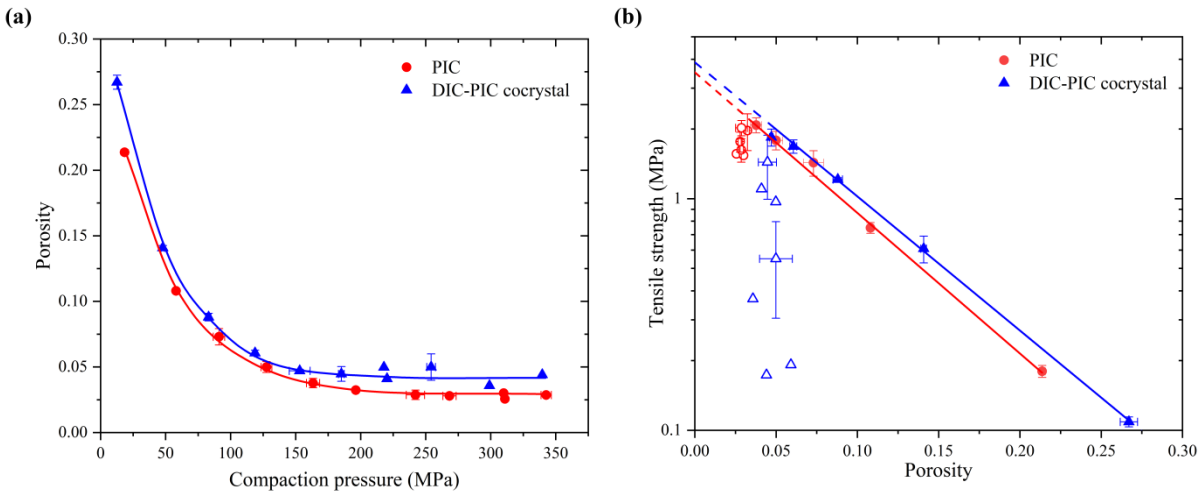

Figure 6. (a) Compressibility and (b) Compactibility profiles of PIC and DIC-PIC cocrystal (n = 3). Over-compressed tablets (open symbols) are not included in the regression.

Table 3. True density, in-die mean yield pressure ($P_{y,i}$) and tensile strength at zero porosity (σ_0) of DIC, PIC, and DIC-PIC cocrystal.

Material	True density (g/cm³)	$P_{y,i}$ (MPa)	σ_0 (MPa)
PIC	1.3252	50.8 ± 0.4	3.51 ± 0.15
DIC	1.4576	86.6 ± 1.4	NA
DIC-PIC	1.3926	59.5 ± 0.6	3.88 ± 0.12

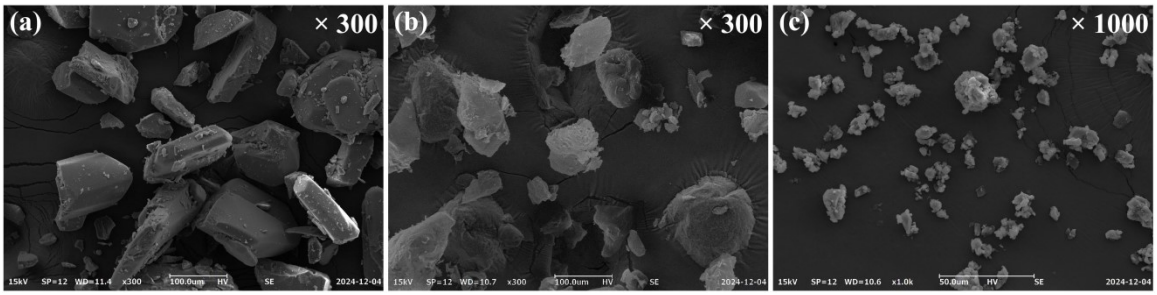

Figure 7. SEM images of crystals compressed (a) DIC, (b) PIC, and (c) DIC-PIC.

3.6. Solubility and IDRs

3.6.1. Solubility

For poorly soluble APIs, such as DIC, solubility often correlates with bioavailability (Chen et al., 2016, Smith et al., 2011, Zhu et al., 2017). The thermodynamic solubility of the DIC-PIC

cocrystal in water (1.57 ± 0.002 mg/mL) is 112 times higher than that of DIC in water (0.0140 ± 0.0001 mg/mL) and 22 times higher in pH = 6.8 buffer solution (9.38 ± 0.01 mg/mL for DIC-PIC vs. 0.43 ± 0.02 mg/mL for DIC) (Table 4). This suggests that DIC-PIC is significantly more soluble than DIC. The solubility of both DIC and DIC-PIC in a pH = 1.2 buffer solution was too low to be detected, suggesting an extremely low intrinsic solubility of DIC in an acidic environment ($pK_a = 4.0 \pm 0.2$ for DIC) (Llinas et al., 2007).

Table 4. Solubility results of DIC and DIC-PIC in water and pH 6.8 buffer (mg/mL, mean ± SD, n=3).

Sample	Water	pH = 6.8
DIC	0.0140 ± 0.0001	0.433 ± 0.016
DIC-PIC cocrystal	1.570 ± 0.002	9.38 ± 0.01

3.6.2. IDRs

It has been shown that the IDR of an API is closely related to its bioavailability (Li et al., 2022). The dissolution plots of both DIC and DIC-PIC are linear, with $R^2 > 0.99$ (0.996 for DIC-PIC and 0.999 for DIC) (Table S3). Thus, IDRs were calculated from corresponding slopes (Figure 8), yielding an IDR of 5.52 ± 0.16 μg/cm²/min for DIC-PIC and 4.13 ± 0.07 μg/cm²/min for DIC. The IDR of the DIC-PIC cocrystal was 1.33 times higher than that of DIC. PXRD results of the exposed tablet surface after the IDR experiments revealed no detectable phase transitions on the pellet surface (Figure S3). This phase stability of DIC-PIC is attributed to the much shorter duration of contact (< 15 min) with the medium during IDR experiment than that during solubility measurement (72 hr).

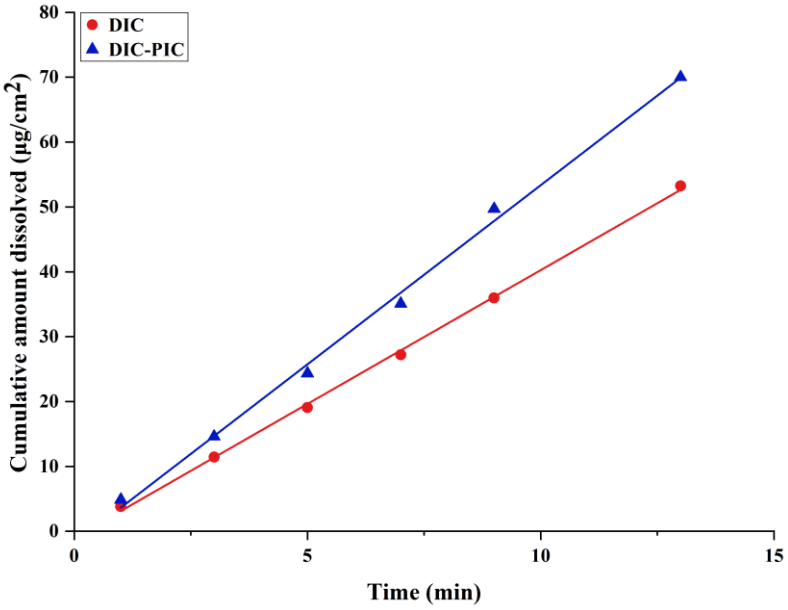

Figure 8. The IDR results of DIC and DIC-PIC cocrystal.

3.7. DVS

The moisture sorption and desorption isotherms of DIC and DIC-PIC showed little moisture uptake up to 95% RH, with maximum mass changes < 0.2% for both (Figure 9). PXRD results of the residual solid after the DVS experiments revealed no detectable phase transitions (Figure S4). Thus, both DIC and DIC-PIC are non-hygroscopic and physically stable against exposure to a high RH (Liu et al., 2021). The mass of DIC-PIC cocrystal was slightly lower than the initial mass after the desorption experiment because of the baseline shift of the balance due to the negligible change in sample mass during the whole cycle.

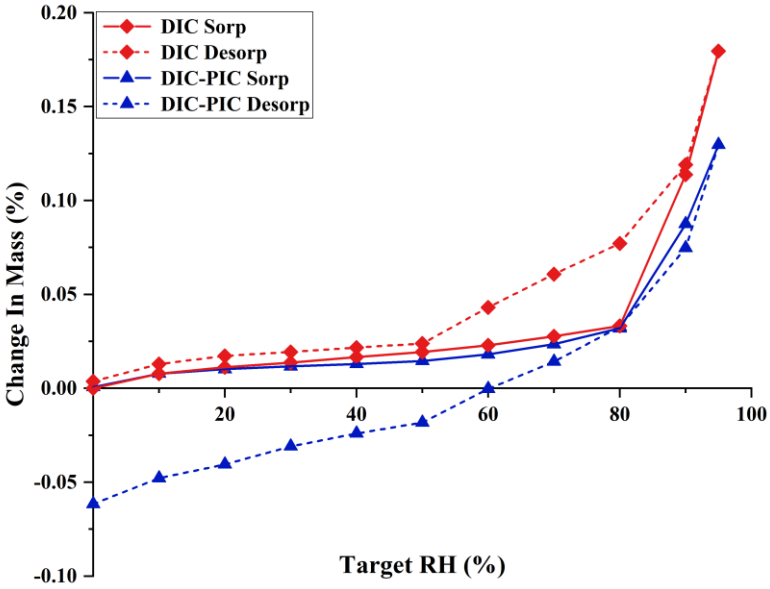

Figure 9. Moisture sorption (solid lines) and desorption (dash lines) profiles of DIC (red) and DIC-PIC cocrystal (blue) at 25 °C.

3.8. Computational calculations

The hydrogen bonded molecular layers can act as slip planes in a crystal, improving powder plasticity and facilitating powder compaction (Sun, 2011). In some cases, identification of the slip planes can be achieved through visual inspection of the crystal structure. However, this may be difficult for more complex crystal structures. An alternative approach is to identify slip planes based on attachment energy, E_{att}, which may contradict the assignment from visual observation (Sun and Kiang, 2008). When a discrepancy between the two methods arises, energy framework can provide more useful information to identify slip planes (Wang and Sun, 2018). In general, slip planes are densely packed molecular layers with the lowest interlayer interaction energy with smoother topology more conducive to slip.

Visualization of the DIC-PIC structure predicts (001) as the primary slip plane (Figure S6a), where intra-layer molecules are mainly connected by halogen bonds (C11-H11···Cl2, 3.629 Å) and the interlayer molecules are connected by $R_4^2(8)$ hydrogen bonds, consisting of C18-H18···C7 (3.558 Å) and C18-H18···C8 (3.732 Å) (Figure 1b, Table S2). The DIC molecules in the (001) plane of DIC-PIC are arranged in an anti-parallel fashion. The slab separation of between adjacent (001)

planes is 0.021 Å, indicating a lack of interdigitation between them (Table S4). This arrangement allows molecular layers to slide along each other even when layer surface is not smooth (Bryant, 2018). The attachment energy (-18.15 kcal/mol, Table S4) of (001) is also the lowest and the (001) facet is the largest of the crystal, occupying 25.0% of the crystal surface area. The assignment of (001) as the slip plane is also supported by energy framework (Figure S5 and 10b), which yields a total intra-layer interaction energy (-78.2 kJ/mol) 36.3% higher than that of inter-layer interaction energy (-49.8 kJ/mol) (Figure S7). The low interlayer interaction energy and high anisotropy explains the high plasticity of DIC-PIC.

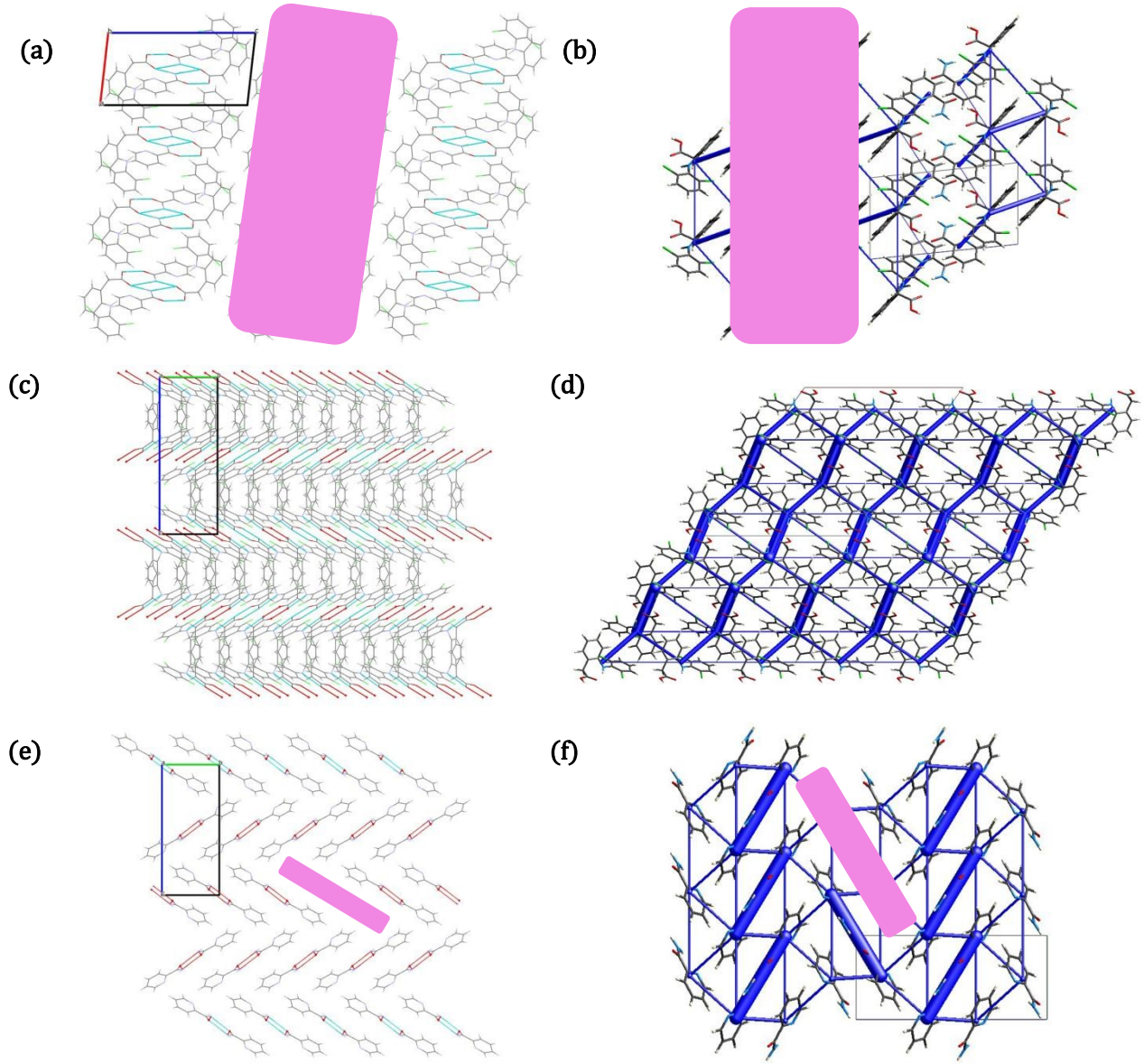

Figure 10. The slip plane and energy frameworks for (a & b) DIC-PIC cocrystal, (c & d) DIC, and (e & f) PIC. A likely slip element (plane or column) is highlighted in pink.

Crystal structure visualization of the DIC crystal reveals the (002) plane as the primary slip plane (Figure S6b), with an attachment energy of 6.953 kcal/mol (Table S5). Based on a comparison of the two energy frameworks, DIC shows much higher intermolecular interaction energy than DIC-PIC cocrystal (Figure 10b and Figure 10d). The total intra-layer energy (-590.0 kJ/mol) of the molecular layer is 9.3% higher than the total inter-layer interaction energy (-534.7 kJ/mol) (Figure S8). In addition, the (002) plane of DIC is stacked along the (200) plane in a wavy shape (Figure S8c), making it difficult for these planes to slide under shear (Raju et al., 2018). The higher inter-layer interaction energy and uneven surface topology explain the lower plasticity of DIC than DIC-PIC.

In the PIC crystal, hydrogen-bonded rigid molecular columns run parallel to the direction of the *a*-axis, i.e., <100> direction (Figure 10e and S9). These molecular columns stack to form a flat layer parallel to the (001) plane. This kind of packing feature is known to favor crystal plasticity because of the lower energy barrier that needs to be overcome for rigid molecular columns to slide than that for a rigid molecular layer (Chattoraj et al., 2010; Chow et al., 2012). This explains the best tabletability and highest plasticity of PIC among the three crystals.

4. Conclusions

A novel DIC-PIC cocrystal prepared in the present study simultaneously improves the tabletability and solubility of DIC. The profoundly improved tabletability of DIC-PIC is consistent with its higher plasticity, which is supported by the presence of slip plane revealed by an analysis of in the crystal structure both visually and computationally. The solubility and IDR of DIC-PIC cocrystal is better than DIC, despite precipitation during prolonged solubility measurement. Overall, the DIC-PIC cocrystal appears to be a better candidate than DIC for the development of a tablet product

CRediT authorship contribution statement

Chenyu Wu: Data curation, Methodology, Writing–original draft. Zijian Wang: Data curation, Writing–review & editing. Xu Han: Data curation. Xinyi Yu: Data curation. Changquan Calvin Sun: Conceptualization, Investigation, Writing–review & editing. Zhengzheng Zhou: Investigation,

Visualization, Supervision, Writing–review & editing.

Declaration of Competing Interest

The authors declare that they have no known competing financial interests or personal relationships that could have appeared to influence the work reported in this paper.

Acknowledgments

This work was supported by the Young Scientists Promotion Fund of Natural Science Foundation of Guangdong Province (no. 2023A1515030128), Natural Science Foundation of Guangdong Province (no. 2024A1515011590) and National Natural Science Foundation of China (no. 81703438). CCS thanks the National Science Foundation for support through the Industry University Collaborative Research Center (IUCRC) grant IIP-2137264, Center for Integrated Materials Science and Engineering for Pharmaceutical Products (CIMSEPP).

References

Aakeröy C. B., Grommet A. B., Desper J., 2011. Co-crystal screening of diclofenac. Pharmaceutics. 3(3), 601-614. https://doi.org/10.3390/pharmaceutics3030601.

Bolla, G., Sarma, B., Nangia, A. K., 2022. Crystal engineering of pharmaceutical cocrystals in the discovery and development of improved drugs. Chem. Rev. 122 (13), 11514-11603. https://doi.org/10.1021/acs.chemrev.1c00987.

Bartolomei, M., Rodomonte, A., Antoniella, E., Minelli, G., Bertocchi, P., 2007. Hydrate modifications of the non-steroidal anti-inflammatory drug diclofenac sodium: solid-state characterisation of a trihydrate form. J. Pharm. Biomed. Anal. 45(3), 443-449. https://doi.org/10.1016/j.jpba.2007.07.002.

Bryant, M. J., Maloney, A. G. P., Sykes, R. A., 2018. Predicting mechanical properties of crystalline materials through topological analysis. CrystEngComm. 20(19), 2698-2704. https://doi.org/10.1039/C8CE00454D.

Chinese pharmacopoeia commission., 2020. Pharmacopoeia of the people's republic of China, fourth ed. China Medical Science Press, Beijing.

Chettri, A., Subba, A., Singh, G. P., Bag, P. P., 2024. Pharmaceutical co-crystals: A green way to enhance drug stability and solubility for improved therapeutic efficacy. J. Pharm. Pharmacol. 76 (1), 1-12. https://doi.org/10.1093/jpp/rgad097.

Cai, L., Farber, L., Zhang, D., Li, F., Farabaugh, J., 2013. A new methodology for high drug loading wet granulation formulation development. Int. J. Pharmaceut. 441 (1-2), 790-800. https://doi.org/10.1016/j.ijpharm.2012.09.052.

Chattoraj, S., Shi, L., Sun, C.C., 2010. Understanding the relationship between crystal structure, plasticity and compaction behaviour of theophylline, methyl gallate, and their 1 : 1 co-crystal. CrystEngComm 12, 2466-2472. https://doi.org/10.1039/C000614A

Chow, S. F., Chen, M., Shi, L., Chow, A. H., Sun, C. C., 2012. Simultaneously improving the mechanical properties, dissolution performance, and hygroscopicity of ibuprofen and flurbiprofen by cocrystallization with nicotinamide. Pharm. Res. 29, 1854-1865. https://doi.org/10.1007/s11095-012-0709-5.

Chen, H., Guo, Y., Wang, C., Dun, J., Sun, C.C., 2019. Spherical cocrystallization—an enabling technology for the development of high dose direct compression tablets of poorly soluble drugs. Cryst. Growth Des. 19 (4), 2503-2510. https://doi.org/10.1021/acs.cgd.9b00219.

Castellari, C., Ottani, S., 1997. Two monoclinic forms of diclofenac acid. Acta. Cryst. 53 (6), 794-797. https://doi.org/10.1107/S0108270197002126.

Chen, Y., Li, L., Yao, J., Ma, Y. Y., Chen, J. M., Lu, T. B., 2016. Improving the solubility and bioavailability of apixaban via apixaban–oxalic acid cocrystal. Cryst. Growth Des. 16 (5), 2923-2930. https://doi.org/10.1021/acs.cgd.6b00266.

Dolomanov, O. V., Bourhis, L. J., Gildea, R. J., Howard, J. A., Puschmann, H., 2009. OLEX2: a complete structure solution, refinement and analysis program. J. Appl. Crystallogr. 42 (2), 339-341. https://doi.org/10.1107/S0021889808042726.

Diniz, L. F., Carvalho, P. S., Jr, Pena, S. A. C., Gonçalves, J. E., Souza, M. A. C., de Souza Filho, J. D., Bomfim Filho, L. F. O., Franco, C. H. J., Diniz, R., Fernandes, C., 2020. Enhancing the solubility and permeability of the diuretic drug furosemide via multicomponent crystal forms. Int. J. Pharmaceut. 587, 119694. https://doi.org/10.1016/j.ijpharm.2020.119694.

Dai, X. L., Pang, B. W., Lv, W. T., Zhen, J. F., Gao, L., Li, C. W., Xiong, J., Lu, T. B., Chen, J. M., 2023. Improving the physicochemical and pharmacokinetic properties of olaparib through cocrystallization strategy. Int. J. Pharmaceut. 647, 123497. https://doi.org/10.1016/j.ijpharm.2023.123497.

Drozd, K. V., Boycov, D. E., Manin, A. N., Churakov, A. V., Perlovich, G. L., 2023. Two novel drug–drug cocrystals of antifungal clotrimazole with nonsteroidal anti-inflammatory drugs. Cryst. Growth Des. 23 (9), 6597-6608. https://doi.org/10.1021/acs.cgd.3c00520.

Duckworth, W., 1953. Discussion of Ryshkewitch paper by Winston Duckworth. J. Am. Ceram. 36,

68–68. https://doi.org/10.1111/j.1151-2916.1953.tb12838.x

Evora, A. O., Castro, R. A., Maria, T. M., Rosado, M. T., Silva, M. R., Canotilho, J., Eusébio, M. E. S., 2012. Resolved structures of two picolinamide polymorphs. Investigation of the dimorphic system behaviour under conditions relevant to co-crystal synthesis. CrystEngComm. 14 (24), 8649-8657. https://doi.org/10.1039/C2CE26244D.

Fell, J. T., Newton, J. M., 1970. Determination of tablet strength by the diametral-compression test. J. Pharm. Sci. 59 (5), 688-691. https://doi.org/10.1002/jps.2600590523.

Feng, W. Q., Wang, L. Y., Gao, J., Zhao, M. Y., Li, Y. T., Wu, Z. Y., Yan, C. W., 2021. Solid state and solubility study of a potential anticancer drug-drug molecular salt of diclofenac and metformin. J. Mol. Struct. 1234, 130166. https://doi.org/10.1016/j.molstruc.2021.130166.

Fael, H., Barbas, R., Prohens, R., Ràfols, C., Fuguet, E., 2021. Synthesis and characterization of a new norfloxacin/resorcinol cocrystal with enhanced solubility and dissolution profile. Pharmaceutics. 14 (1), 49. https://doi.org/10.3390/pharmaceutics14010049.

Gaitano, R. O., Calvo, N. L., Narda, G. E., Kaufman, T. S., Maggio, R. M., Brusau, E. V., 2016. Preparation and physical characterization of a diclofenac-ranitidine co-precipitate for improving the dissolution of diclofenac. J. Pharm. Sci. 105 (3), 1258-1268. https://doi.org/10.1016/j.xphs.2016.01.001.

Goswami, P. K., Kumar, V., Ramanan, A., 2020. Multicomponent solids of diclofenac with pyridine based coformers. J. Mol. Struct. 1210, 128066. https://doi.org/10.1016/j.molstruc.2020.128066.

Good, D. J., Rodríguez-Hornedo, N., 2009. Solubility advantage of pharmaceutical cocrystals. Cryst. Growth Des. 9(5), 2252-2264. https://doi.org/10.1021/cg801039j.

Gupta, H., Bhandari, D., Sharma, A., 2009. Recent trends in oral drug delivery: a review. Recent. Pat. Drug. Deliv. Formul. 3 (2), 162-173. https://doi.org/10.2174/187221109788452267

Goldenberg, M., Vreeman, G., Sun, D.J., Moffit, M., Li, M., Zernik, M., Ahuja, S., Kim, Y., Semin, D., Sun, C.C., 2023. A material-sparing simplified buoyancy method for determining the true density of solids. Int. J. Pharmaceut. 635, 122694. https://doi.org/10.1016/j.ijpharm.2023.122694.

Ghosh, S., Mishra, M. K., 2021. Elastic molecular crystals: From serendipity to design to applications. Cryst. Growth Des. 21(4), 2566-2580. https://doi.org/10.1021/acs.cgd.0c01743.

Hao, X., Li, J., Wang, C., Zhao, X., He, X., Sun, C. C., 2022. Profoundly improved photostability of dimetronidazole by cocrystallization. CrystEngComm. 24 (35), 6165-6171.

https://doi.org/10.1039/d2ce00597b.

Heckel, W., 1961. An analysis of powder compaction phenomena. Trans. Metall. Soc. AIME. 221, 671-675.

Hiew, B. Y. Z., Lee, L. Y., Lai, K. C., Gan, S., Thangalazhy-Gopakumar, S., Pan, G. T., Yang, T. C, 2019. Adsorptive decontamination of diclofenac by three-dimensional graphene-based adsorbent: response surface methodology, adsorption equilibrium, kinetic and thermodynamic studies. Environ. Res. 168, 241-253. https://doi.org/10.1016/j.envres.2018.09.030.

Hui, R., Guan, C., Hou, D. Y., 2001. Study on IR characteristics of carboxylic acid and their salts. J. Anshan. Teach. Coll. 3 (1), 95-98. https://kns.cnki.net/.

Joiris, E., Martino, P. D., Berneron, C., Guyot-Hermann, A. M., Guyot, J. C., 1998. Compression behavior of orthorhombic paracetamol. Pharm. Res. 15, 1122-1130. https://doi.org/10.1023/A:1011954800246.

Joseph, J., Jemmis, E. D., 2007. Red-, blue-, or no-shift in hydrogen bonds: a unified explanation. J. Am. Chem. Soc. 129(15), 4620-4632. https://doi.org/10.1021/ja067545z.

Karki, S., Friščić, T., Fábián, L., Laity, P. R., Day, G. M., Jones, W., 2009. Improving mechanical properties of crystalline solids by cocrystal formation: new compressible forms of paracetamol. Adv. Mater. 21 (38-39), 3905-3909. https://doi.org/10.1002/adma.200900533.

Kuentz, M., Leuenberger, H., 1999. Pressure susceptibility of polymer tablets as a critical property: a modified Heckel equation. J. Pharm. Sci. 88 (2), 174-179. https://doi.org/10.1021/js980369a.

Kumari, N., Roy, P., Roy, S., Wang, C., Das, S., Pandey, N., Mondal, S.K., Bose, A., Sun, C.C., Ghosh, A., 2024. Development of direct compression Acetazolamide tablet with improved bioavailability in healthy human volunteers enabled by cocrystallization with p-Aminobenzoic acid. Int. J. Pharmaceut. 652, 123793. https://doi.org/10.1016/j.ijpharm.2024.123793.

Li, J., Song, S., Huang, W., Fan, H., Zhou, Z., 2023. Novel drug-drug salts of enoxacin with enhanced antibacterial activity: insights from solubility and lipid-water partition coefficient. J. Mol. Liq. 122443. https://doi.org/10.1016/j.molliq.2023.122443.

Li, J., Huang, Y., An, Q., Li, W., Li, J., Liu, H., Yang, D., Lu, Y., Zhou, Z., 2022. Discovered two polymorphs and two solvates of lamotrigine-tolfenamic acid salt: thermal behavior and crystal morphological differences. Int. J. Pharmaceut. 628, 122310. https://doi.org/10.1016/j.ijpharm.2022.122310.

Liu, H., Nie, J., Stephen Chan, H. C., Zhang, H., Li, L., Lin, H., Tong, H. H. Y., Ma, A., Zhou, Z., 2021. Phase solubility diagrams and energy surface calculations support the solubility enhancement with low hygroscopicity of bergenin: 4-aminobenzamide (1:1) cocrystal. Int. J. Pharmaceut. 601, 120537. https://doi.org/10.1016/j.ijpharm.2021.120537.

Llinas, A., Burley, J. C., Box, K. J., Glen, R. C., Goodman, J. M., 2007. Diclofenac solubility: independent determination of the intrinsic solubility of three crystal forms. J. Med. Chem. 50 (5), 979-983. https://doi.org/10.1021/jm0612970.

Lemmerer, A., Adsmond, D. A., Esterhuysen, C., Bernstein, J., 2013. Polymorphic co-crystals from polymorphic co-crystal formers: competition between carboxylic acid···pyridine and phenol···pyridine hydrogen bonds. Cryst. Growth Des. 13(9), 3935-3952. https://doi.org/10.1021/cg4006357.

Mannava, M. C., Gunnam, A., Lodagekar, A., Shastri, N. R., Nangia, A. K., Solomon, K. A., 2021. Enhanced solubility, permeability, and tabletability of nicorandil by salt and cocrystal formation. CrystEngComm. 23 (1), 227-237. https://doi.org/10.1039/D0CE01316A.

Mukherjee, A., Tothadi, S., Chakraborty, S., Ganguly, S., Desiraju, G. R., 2013. Synthon identification in co-crystals and polymorphs with IR spectroscopy. Primary amides as a case study. CrystEngComm. 15(23), 4640-4654. https://doi.org/10.1039/C3CE40286J.

Mackenzie, C. F., Spackman, P. R., Jayatilaka, D., Spackman, M. A., 2017. CrystalExplorer model energies and energy frameworks: extension to metal coordination compounds, organic salts, solvates and open-shell systems. IUCrJ. 4 (5), 575-587. https://doi.org/10.1107/S205225251700848X.

Modi, S. R., Khomane, K. S., Bansal, A. K., 2014. Impact of differential surface molecular environment on the interparticulate bonding strength of celecoxib crystal habits. Int. J. Pharmaceut. 460 (1-2), 189-195. https://doi.org/10.1016/j.ijpharm.2013.10.029.

Nugrahani, I., Utami, D., Ibrahim, S., Nugraha, Y. P., Uekusa, H., 2018. Zwitterionic cocrystal of diclofenac and L-proline: structure determination, solubility, kinetics of cocrystallization, and stability study. Eur. J. Pharm. Sci. 117, 168-176. https://doi.org/10.1016/j.ejps.2018.02.020.

Pandey, N., Kumari, N., Roy, P., Mondal, S. K., Thakur, A., Sun, C. C., Ghosh, A., 2024. Tuning Caco-2 permeability by cocrystallization: Insights from molecular dynamics simulation. Int. J. Pharmaceut. 650, 123666. https://doi.org/10.1016/j.ijpharm.2023.123666.

Perumalla, S. R., Sun, C. C., 2014. Enabling tablet product development of 5-fluorocytosine through integrated crystal and particle engineering. J. Pharm. Sci. 103 (4), 1126-1132. https://doi.org/10.1002/jps.23876.

Pireddu, R., Sinico, C., Ennas, G., Schlich, M., Valenti, D., Murgia, S., Marongiu, F., Fadda, A. M., Lai, F., 2018. The effect of diethylene glycol monoethyl ether on skin penetration ability of diclofenac acid nanosuspensions. Colloids. Surf. B. 162, 8-15. https://doi.org/10.1016/j.colsurfb.2017.11.012.

Paradkar, A. R., Pawar, A. P., 2010. Crystallo-co-agglomeration: A novel particle engineering technique. AJP. 4(1). https://doi.org/10.4103/0973-8398.63975.

Pérez-Estrada, L. A., Malato, S., Gernjak, W., Agüera, A., Thurman, E. M., Ferrer, I., Fernández-Alba, A. R., 2005. Photo-Fenton degradation of diclofenac: identification of main intermediates and degradation pathway. Environ. Sci. Technol. 39 (21), 8300-8306. https://doi.org/10.1021/es050794n.

Perlovich, G. L., 2015. Thermodynamic characteristics of cocrystal formation and melting points for rational design of pharmaceutical two-component systems. CrystEngComm. 17 (37), 7019-7028. https://doi.org/10.1039/C5CE00992H.

Patel, S., Kaushal, A. M., Bansal, A. K., 2006. Compression physics in the formulation development of tablets. Crit. Rev. Ther. Drug Carrier Syst. 23 (1), 1-65. https://doi.org/10.1615/critrevtherdrugcarriersyst.v23.i1.10.

Ramirez, M., 2010. Molecular architecture influences on material properties of pharmaceutical compounds. Diss. Aston University.

Raju, K. B., Ranjan, S., Vishnu, V. S., Bhattacharya, M., Bhattacharya, B., Mukhopadhyay, A. K., Reddy, C. M., 2018. Rationalizing distinct mechanical properties of three polymorphs of a drug adduct by nanoindentation and energy frameworks analysis: role of slip layer topology and weak interactions. Cryst. Growth Des. 18(7), 3927-3937. https://doi.org/10.1021/acs.cgd.8b00261.

Ryshkewitch, E., 1953. Compression strength of porous sintered alumina and zirconia. J. Am. Ceram. 36, 65–68. https://doi.org/10.1111/j.1151-2916.1953.tb12837.x

Sun, C. C., 2009. Materials science tetrahedron —— A useful tool for pharmaceutical research and development. J. Pharm. Sci. 98 (5), 1671-1687. https://doi.org/10.1002/jps.21552.

Sheldrick, G. M., 2015. SHELXT–Integrated space-group and crystal-structure determination. Acta. Crystallogr. A. 71 (1), 3-8. https://doi.org/10.1107/S2053273314026370.

Semalty, A., Semalty, M., Singh, D., Rawat, M. S. M., 2009. Development and physicochemical evaluation of pharmacosomes of diclofenac. Acta. Pharmaceutica. 59 (3), 335-344. https://doi.org/10.2478/v10007-009-0023-x.

Shaikh, R., Singh, R., Walker, G. M., Croker, D. M., 2018. Pharmaceutical cocrystal drug products: an outlook on product development. TIPS. 39 (12), 1033–1048. https://doi.org/10.1016/j.tips.2018.10.006.

Surov, A. O., Voronin, A. P., Manin, A. N., Manin, N. G., Kuzmina, L. G., Churakov, A. V., Perlovich, G. L., 2014. Pharmaceutical cocrystals of diflunisal and diclofenac with theophylline. Mol. Pharmaceutics. 11 (10), 3707-3715. https://doi.org/10.1021/mp5004652.

Saha, S., Desiraju, G. R., 2018. Acid···Amide supramolecular synthon in cocrystals: from spectroscopic detection to property engineering. J. Am. Chem. Soc. 140 (20), 6361-6373. https://doi.org/10.1021/jacs.8b02435.

Sun, C.C., 2005. Quantifying errors in tableting data analysis using the Ryshkewitch equation due to inaccurate true density. J. Pharm. Sci. 94, 2061–2068. https://doi.org/10.1002/jps.20421

Sun, C. C., Kiang, Y. H., 2008. On the identification of slip planes in organic crystals based on attachment energy calculation. J. Pharm. Sci. 97 (8), 3456-3461. https://doi.org/10.1002/jps.21234.

Spackman, P. R., Turner, M. J., McKinnon, J. J., Wolff, S. K., Grimwood, D. J., Jayatilaka, D., Spackman, M. A., 2021. CrystalExplorer: a program for Hirshfeld surface analysis, visualization and quantitative analysis of molecular crystals. J. Appl. Cryst. 54 (3), 1006-1011. https://doi.org/10.1107/S1600576721002910.

Schultheiss, N., Newman, A., 2009. Pharmaceutical cocrystals and their physicochemical properties. Cryst. Growth Des. 9 (6), 2950-2967. https://doi.org/10.1021/cg900129f.

Sun, C. C., 2017. Microstructure of tablet-pharmaceutical significance, assessment, and engineering. Pharm. Res. 34, 918-928. https://doi.org/10.1007/s11095-016-1989-y.

Sun, C. C., Kleinebudde, P., 2016. Mini review: Mechanisms to the loss of tabletability by dry granulation. Eur. J. Pharm. Biopharm. 106, 9-14. https://doi.org/10.1016/j.ejpb.2016.04.003.

Sun, C. C., 2009. Materials science tetrahedron—A useful tool for pharmaceutical research and development. J. Pharm. Sci. 98 (5), 1671-1687. https://doi.org/10.1002/jps.21552.

Smith, B. C., 2018. The C=O bond, part III: Carboxylic Acids. Spectroscopy. 33, 14-20.

Takei, K., R. Takahashi and T. Noguchi, 2008. Correlation between the hydrogen-bond structures and the C=O stretching frequencies of carboxylic acids as studied by density functional theory calculations: theoretical basis for interpretation of infrared bands of carboxylic groups in proteins. J. Phys. Chem. B. 112(21), 6725-6731.

https://doi.org/10.1021/jp801151k.

Surov, A. O., Voronin, A. P., Vener, M. V., Churakov, A. V., Perlovich, G. L., 2018. Specific features of supramolecular organisation and hydrogen bonding in proline cocrystals: a case study of fenamates and diclofenac. CrystEngComm. 20 (43), 6970-6981. https://doi.org/10.1039/C8CE01458B.

Sun, C. C., 2011. Decoding powder tabletability: roles of particle adhesion and plasticity. J. Adhes. Sci. Technol. 25 (4-5), 483-499. https://doi.org/10.1163/016942410X525678.

Smith, A. J., Kavuru, P., Wojtas, L., Zaworotko, M. J., Shytle, R. D., 2011. Cocrystals of quercetin with improved solubility and oral bioavailability. Mol. Pharmaceutics. 8 (5), 1867-1876. https://doi.org/10.1021/mp200209j.

Varshosaz, J., Ghassami, E., Ahmadipour, S., 2018. Crystal engineering for enhanced solubility and bioavailability of poorly soluble drugs. Curr. Pharm. Des. 24 (21), 2473-2496. https://doi.org/10.2174/1381612824666180712104447.

Vreeman, G., Sun, C. C., 2021. Mean yield pressure from the in-die Heckel analysis is a reliable plasticity parameter. Int. J. Pharmaceut. 3, 100094. https://doi.org/10.1016/j.ijpx.2021.100094.

Wang, K., Hao, Y., Wang, C., Zhao, X., He, X., Sun, C. C., 2022. Simultaneous improvement of physical stability, dissolution, bioavailability, and antithrombus efficacy of Aspirin and Ligustrazine through cocrystallization. Int. J. Pharmaceut. 616, 121541. https://doi.org/10.1016/j.ijpharm.2022.121541.

Wang, C., Sun, C. C., 2018. Identifying slip planes in organic polymorphs by combined energy framework calculations and topology analysis. Cryst. Growth Des. 18 (3), 1909-1916. https://doi.org/10.1021/acs.cgd.8b00202.

Wang, C., Sun, C. C., 2019. Computational techniques for predicting mechanical properties of organic crystals: a systematic evaluation. Mol. Pharmaceutics. 16 (4), 1732-1741. https://doi.org/10.1021/acs.molpharmaceut.9b00082.

Wang, C., Paul, S., Wang, K., Hu, S., Sun, C. C., 2017. Relationships among crystal structures, mechanical properties, and tableting performance probed using four salts of diphenhydramine. Cryst. 17 (11), 6030-6040. https://doi.org/10.1021/acs.cgd.7b01153.

Wang, Z., Wang, C., Guo, Y., Bahl, D., Fok, A., Sun, C. C., 2024. A new insight into the mechanism of the tabletability flip phenomenon. Int. J. Pharmaceut. 123956. https://doi.org/10.1016/j.ijpharm.2024.123956.

Wang, Z., Wang, C., Bahl, D., Sun, C. C., 2023. The ubiquity of the tabletability flip phenomenon. Int. J. Pharmaceut. 643, 123262. https://doi.org/10.1016/j.ijpharm.2023.123262.

Xu, K., Xiong, X., Guo, L., Wang, L., Li, S., Tang, P., Yan, J., Wu, D., Li, H., 2015. An investigation into the polymorphism and crystallization of levetiracetam and the stability of its solid form. J. Pharm. Sci. 104 (12), 4123-4131. https://doi.org/10.1002/jps.24628.

Yadav, J. A., Khomane, K. S., Modi, S. R., Ugale, B., Yadav, R. N., Nagaraja, C. M., Kumar, N., Bansal, A. K., 2017. Correlating single crystal structure, nanomechanical, and bulk compaction behavior of febuxostat polymorphs. Mol. Pharmaceutics. 14 (3), 866–874. https://doi.org/10.1021/acs.molpharmaceut.6b01075.

Zhang, Q., Xia, M., Zheng, C., Yang, Y., Bao, J., Dai, W., Mei, X., 2023. The cocrystal of ubiquinol: improved stability and bioavailability. Pharmaceutics. 15 (10), 2499. https://doi.org/10.3390/pharmaceutics15102499.

Zhou, Z., Li, W., Sun, W. J., Lu, T., Tong, H. H. Y., Sun, C. C., Zheng, Y., 2016a. Resveratrol cocrystals with enhanced solubility and tabletability. Int. J. Pharmaceut. 509 (1-2), 391-399. https://doi.org/10.1016/j.ijpharm.2016.06.006.

Zhou, F., Zhou, J., Zhang, H., Tong, H. H., Nie, J., Li, L., Zhang, Y., Du, J., Ma, A., Yang, X., Zhou, Z., 2019. Structure determination and in vitro/vivo study on carbamazepine-naringenin (1:1) cocrystal. J. Drug Delivery Sci. Technol. 54, 101244. https://doi.org/10.1016/j.jddst.2019.101244.

Zhou, J., Li, L., Zhang, H., Xu, J., Huang, D., Gong, N., Han W., Yang X., Zhou, Z., 2020. Crystal structures, dissolution and pharmacokinetic study on a novel phosphodiesterase-4 inhibitor chlorbipram cocrystals. Int. J. Pharmaceut. 576, 118984. https://doi.org/10.1016/j.ijpharm.2019.118984.

Zhu, B., Zhang, Q., Wang, J. R., Mei, X., 2017. Cocrystals of baicalein with higher solubility and enhanced bioavailability. Cryst. Growth Des. 17 (4), 1893-1901. https://doi.org/10.1021/acs.cgd.6b01863.

Zhou, Z., Chan, H. M., Sung, H. H. Y., Tong, H. H., Zheng, Y., 2016b. Identifification of new cocrystal systems with stoichiometric diversity of salicylic acid using thermal methods. Pharm. Res. 33, 1030-1039. https://doi.org/10.1007/s11095-015-1849-1.

Zhu, Y., Lin, Q., Fan, H., Zhang, L., Yang, S., Yang, D., Lu, Y., Zhou, Z., 2024. Novel Spherical Trimethoprim–Niflumic Acid Drug–Drug Salt Demonstrates Simultaneous Enhancement of Powder Property and Antibacterial Activity. Cryst. Growth Des. 2024, 24, 5324−5334. https://doi.org/10.1021/acs.cgd.4c00562.